Appl Phys A (2009) 94: 675–690
DOI 10.1007/s00339-008-4958-4

Applied Physics A
Materials Science & Processing

Dynamics evolution of shock waves in laser–material interaction

Sobieslaw Gacek · Xinwei Wang

Received: 14 May 2008 / Accepted: 24 October 2008 / Published online: 12 November 2008

Abstract In this work, the dynamics and internal structure of shock waves in picosecond laser–material interaction are explored at the atomistic level. The pressure of the shock wave, its propagation, and interaction zone thickness between the plume and ambience are evaluated to study the effect of the laser absorption depth, ambient pressure, and laser fluence. Sound agreement is observed between the MD simulation and theoretical prediction of shock wave propagation and mass velocity. Due to the strong constraint from the compressed ambient gas, it is observed that the ablated plume could stop moving forward and mix with the ambient gas, or move backward to the target surface, leading to surface redeposition. Under smaller laser absorption depth, lower ambient pressure, or higher laser fluence, the shock wave will propagate faster and have a thicker interaction zone between the target and ambient gas.

PACS 47.40.Nm · 52.38.-r · 87.10.Tf

1 Introduction

Over the past two decades, there has been immense interest in laser ablation [1, 2] of materials and tremendous developments in one of its derivative techniques, well recognized as pulsed laser deposition (PLD) [3]. Considerable success of this method comes with its expanding applications, relatively high efficiency, and extreme versatility of advantageous offering features for depositing high-quality thin films of many new materials, including dielectrics and superconductors. The PLD process constitutes a sequence of particularly convoluted and multiplex phenomena inclusive of laser–solid interaction, evaporation/explosion of target material, and consequent plasma plume formation. It is almost certain that transportation and evolution of the intense, very short time scale shock waves associated with intense processes in the plume front will further take place, along with plume–solid interaction at the deposited surface. Of special importance and intricacy is the dynamics evolution of shock waves in laser–material interaction. When a background gas instead of a vacuum environment is present, considerable new processes arise, such as deceleration, attenuation and thermalization of the molten particles, as well as diffusion, recombination and formation of the shock waves [4]. Often observables are also generation of multiple fronts, nanoclusters frequently combined with plume backward motion occurrence, and the phenomenon of 'plume splitting', all resulting in significant impact on the deposition process.

The nanoscale shock wave phenomenon has long fascinated researchers all around the world and has been the subject of intensive investigation in recent years. The issue of plume splitting in low pressure background gases has been reported in the profound experimental [5, 6] and numerical work by Geohegan et al. [7, 8]. The work by Voevodin et al. [9] presents results of laser ablation deposition of yttria stabilized zirconia films in a low pressure oxygen and argon ambient environment. One significant study by Harilal et al. [10] shows the effect of ambient air pressure on the expansion dynamics of the plasma generated by laser ablation of an aluminum target. Mason and Mank [11] investigated how laser parameters, especially laser fluences, affect crater size and shape formation. Moreover, Russo et al. [12, 13]

S. Gacek · X. Wang (✉)
Department of Mechanical Engineering, Iowa State University, 2010 H. M. Black Engineering Building, Ames, IA 50011-2161, USA
e-mail: xwang3@iastate.edu
Fax: +1-515-2943261

performed sound research on how laser fluence, the induced recoil pressure, and radiating heating of the substrate influence the amount of ablated material mass.

The subject of laser ablation is also extensively treated in prior theoretical and numerical literature. The analysis of multiple shock waves has been well documented in a theoretical study by Bulgakov and Bulgakova [14]. In Le et al.'s study [4], the physical phenomena involved in laser-induced plasma expansion into a background gas was numerically studied. The authors developed a model which considers diffusions, thermal conduction, viscosity, and ionization effects. A new theoretical model has been developed by Zhang and Gogos [15] to explain the influence of ambient gas and laser intensity in laser ablation. Another theoretical study by Bulgakov [16] paid particular attention to the analogy between an ablation plume and a supersonic under-expanded gaseous jet.

Although a substantial amount of research on laser ablation has been conducted, the underlying effects and the mechanism of laser induced plume expansion in an ambient environment still remains relatively unclear. To gain further insights into these fascinating phenomena, molecular dynamics (MD) simulation is necessary, which allows direct tracking of the movement of molecules/atoms. Additionally, this method is capable of revealing the thermally induced processes down to atomistic levels in laser–surface nanostructuring [17]. A vast amount of commitment has been devoted to the usage of MD to study laser–material interaction; of special significance is the work by Zhigilei et al. [18]. Zhigilei's in-depth study revealed a number of physical phenomena, including temperature and pressure evolution, phase change/explosion, structural change, and ablation rate change in laser ablation of molecular systems including organic materials. Investigations on thermal transport, phase change, thermal stress development and propagation, and nanoparticle formation in laser–material interaction can also be found in other papers [17, 19–21]. It needs to be pointed out that in these MD studies of laser–material interaction the emphasis was placed on the plume behavior during laser ablation in vacuum (without shock wave). The effect of shock wave on plume evolution has not been studied in these works.

In recent years, more emphases have been placed on the exploration of kinetic and physical properties of nano-domain shock wave [22] and its dynamic structure with mass penetration [23]. Nevertheless, none of those papers fully described shock wave formation, propagation and attenuation, interaction of the shock wave with the ablation plume, the effect of the optical absorption depth on the shock wave, or the effect of the laser pulse width, laser fluence, background pressure, and species of the background gas. It would be of considerable significance to have a compendium of those compelling processes. In this paper, we present quantitative explanations for a number of gas-dynamics effects when the interaction between the picosecond laser ablated argon plume and background gas occurs in a very short time—up to 5 ns.

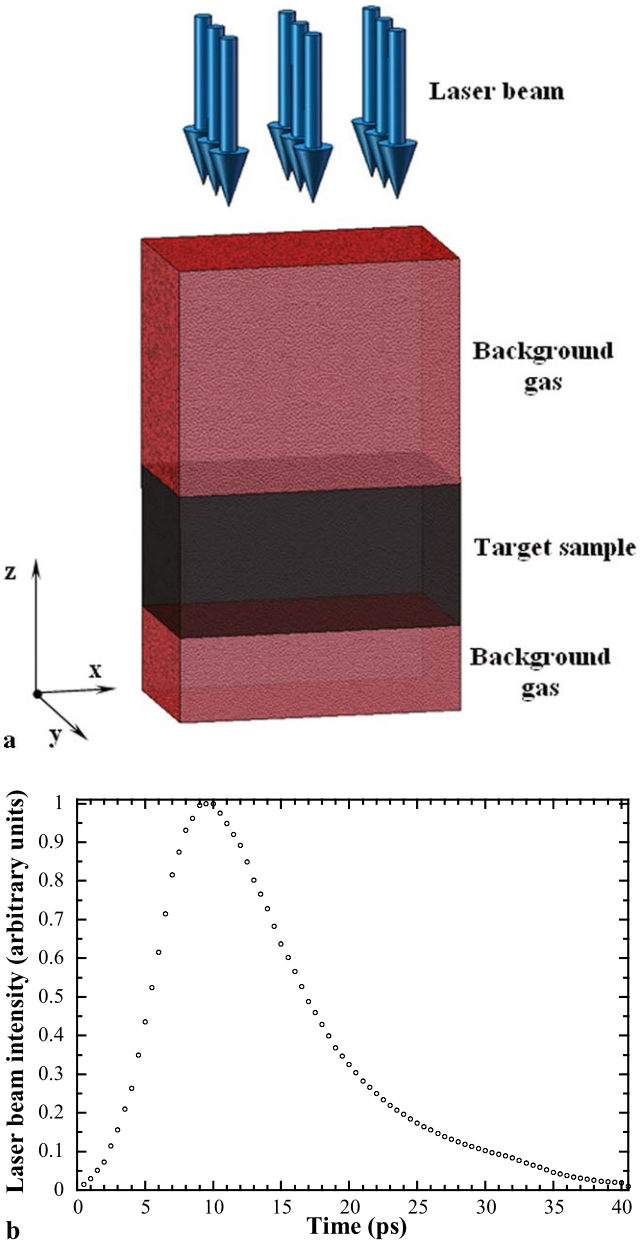

Fig. 1 **a** A schematic of the domain construction for shock wave simulation; **b** temporal distribution of the laser intensity

2 Methodologies of simulation

For the purpose of this study, the computational domain has been designed to resemble a free-standing target material placed in a gas environment irradiated by a laser pulse (Fig. 1a). Argon material is selected for the film target in the

simulations because it is well characterized physically and chemically, and it has been thoroughly studied in the laser–material interaction using MD. Argon crystal structure as the target has an initial temperature of 50 K, and the lattice constant a of the face-centered-cube (fcc) is 5.414 Å. The background gas shares similar properties, such as the molecular mass, as the target but has a modified interatomic potential which considers only repulsive force between atoms. Except for this, the model gas is arranged to have the same parameters as argon for MD simulation. As a result, this approach significantly simplifies the computation and reduces computational time. The basic problem of MD simulation involves solving the Newtonian equation for each atomic pair interaction with the usage of the Lennard–Jones potential:

$$m_i \frac{d^2 r_i}{dt^2} = \sum_{j \neq i} F_{ij}, \tag{1}$$

where m_i and r_i are the mass and position of atom i, respectively, F_{ij} is the pair force between atoms i and j which is calculated as $F_{ij} = -\partial \phi_{ij} / \partial r_{ij}$. The Lennard–Jones (12–6) potential is in the form given by

$$\phi_{ij} = 4 \cdot \varepsilon \left[\left(\frac{\sigma}{r_{ij}} \right)^{12} - \left(\frac{\sigma}{r_{ij}} \right)^{6} \right], \tag{2}$$

where $\varepsilon = 1.653 \times 10^{-21}$ J is the LJ well depth parameter for argon, $\sigma = 3.406$ Å is referred to as the equilibrium separation parameter, and $r_{ij} = r_i - r_j$. In this calculation, a time step of 25 fs is used, and (1) is solved by applying the modified Verlet algorithm to the velocity, which is commonly identified as the half-step leap-frog scheme [25]. The interaction between atoms is neglected when their distance is beyond the cutoff distance (2.5σ). For more computational details and parameter specifications, readers are advised to see further explanations in Wang's previous work [17, 19–21]. The computational domain measures $32.5 \times 2.7 \times 3627$ (nm) ($x \times y \times z$) and consists of 375 000 atoms. The solid target material is 108 nm long in the z-direction, below which there is a 271 nm long gas domain. Periodic boundary conditions are imposed to the boundaries in the x- and y-directions, and free boundary conditions to the boundaries in the z-direction.

The target top surface is uniformly irradiated with a single laser pulse which has a temporal Gaussian distribution (Fig. 1b) and a fluence of 3 J/m^2. During the first 200 ps (8000 steps), the velocity of molecules is being scaled up to 100 ps until the sample reaches 50 K. Then equilibrium calculation is conducted to make sure that the disturbance caused by the velocity scaling is eliminated. Towards the end of the equilibration, the ambient gas reaches a pressure of 0.22 MPa, close to the ideal gas condition (0.27 MPa). In this work, different ambient pressures ranging from 0.051 MPa to 0.87 MPa are used for studying shock waves. These pressures are higher than those used in PLD, and are close to open-air laser-assisted surface nanostructuring, and pulsed laser-assisted material machining (polishing, welding, and drilling). The reported results are designed to study the early stage shock wave dynamic behavior rather than to recover an experimental condition.

After 200 ps equilibrium calculation, the laser beam heating is applied on the top target surface, and the laser beam is volumetrically absorbed in the material. This incident laser beam within each time step (δt) is assumed to be absorbed exponentially with an artificial optical absorption depth (τ) and is expressed by the following formula [17]

$$\frac{dI}{dz} = -\frac{I(z)}{\tau}. \tag{3}$$

The incident laser energy within a time step (δt) is $E_1 = \delta t \cdot I \cdot A$, where A is the area of the target surface. The laser energy absorbed inside the material is

$$\Delta E = E_0 \cdot \left(1 - \exp\left[-\frac{\delta z}{\tau_0} \right] \right), \tag{4}$$

where δz is the layer thickness, and E_0 is the energy incident on one single layer in the z-direction. The domain is divided into such layers whose thicknesses are a little larger than the cutoff distance used in force calculation. $\tau_0 = \tau \cdot \rho_0 / \rho$ is the adjusted real optical absorption depth, where ρ_0 and ρ are the bulk density and true density of the target, respectively. Finally, laser beam absorption in the target is achieved by exciting the kinetic energy of atoms, and is accomplished by scaling the velocities of atoms by a factor which is expressed by [17]

$$\chi = \left\{ 1 + \frac{\Delta E}{\frac{1}{2} \sum_{i=1}^{N} m_i \cdot ((v_{i,1} - \bar{v}_1)^2 + (v_{i,2} - \bar{v}_2)^2 + (v_{i,3} - \bar{v}_3)^2)} \right\}^{0.5}, \tag{5}$$

where $v_{i,j}$ and $\bar{v}_j$ ($j = 1, 2, 3$) are the velocities of atom i and the average velocity in the x-, y-, and z-directions for atoms in a layer normal to the laser beam. The new velocity, $v'_{i,j}$, of atom i is calculated as

$$v'_{i,j} = (v_{i,j} - \bar{v}_j) \cdot \chi + \bar{v}_j, \quad j = 1, 2, 3. \tag{6}$$

Moreover, in the simulations conducted in this work a force elimination procedure needs to be considered as follows. In laser interaction with the target material, a strong stress wave will form and propagate throughout the target in the laser incident direction. When this laser-induced stress wave reaches the opposite side of the target, it can tear off the material and induce unrealistic damage, or the stress wave can be reflected and may induce unexpected artifacts in the liquid–vapor zone, causing changes in the generation and behavior of the shock wave. In our approach, a special

boundary treatment is used at the back side of the target to eliminate the above phenomena. A terminating force is applied to the atoms in the affected boundary region, and it can be expressed following the work by Zhigilei and Garison [24] as:

$$F_t = -\frac{\rho \cdot v \cdot c \cdot A}{N}, \tag{7}$$

where ρ is the density of the target in the selected region, v is the instantaneous average velocity of the atoms within the boundary, and c is the speed of propagating stress wave. N is the number of molecules/atoms confined by the affected region. Wang's previous simulations [23] proved that the above stress boundary treatment works well in terms of eliminating stress wave reflection and avoiding undesired material damage in the boundary region.

3 Results and discussion

3.1 Shock wave formation and evolution: the general picture

Consideration of the shock wave formation and evolution is presented on the basis of the situation when the laser energy is 3 J/m^2, the absorption depth is 5 nm, and ambient gas pressure is slightly above 2 atm. A series of snapshots of atomic positions in the simulated domain (x–z plane) at different times are shown in Fig. 2a. At 0.5 ns a denser region in red is already visible, which represents the expansion front of the shock wave (marked with arrows). The applied laser beam forces the target material to evaporate because its energy intensity exceeds the material ablation threshold, leading to the generation of an evidently strong shock wave composed of compressed adjacent gas above the target. During the initial stages, the ejected plume immediately exerts forward, being induced by the high pressure mainly from the intense phase explosion [21] and expands into the background gas until the end of laser pulse. As can be noticed in later stages, nanoparticle-like clusters are formed, mainly due to the phase explosion and condensation [10]. When the high energy plume propagates through the background gas, the interrelation between solid and gas becomes more significant. More mass of the ambient gas is being entrained in the shock wave front. Meanwhile, the ejected plume is being restrained due to increasing repulsive effect from the ambient gas. This restraint prevents the plume from developing freely in space. Consequently, thermalization of the plume occurs because slowing of the plume velocity converts its kinetic energy into thermal energy.

With the time evolving, the co-existing length between the plume and the background gas increases because of the relative movement between the plume and the ambient gas. A very interesting phenomenon observed in Fig. 2a is that starting from 3 ns the expansion of the plume in space is significantly slowed down. Moreover, some of the particles/clusters in the plume start to move down toward the target surface although the shock wave front continues to propagate out. This type of backward movement of the plume is being studied in our group by further processing the MD data of a wide spectrum of calculations. From 3 to 5 ns, it is also observed that some clusters/particles stop moving out. Instead, they float and mix with the ambient gas.

3.2 Atomic velocity inside the shock wave

For shock waves generated in laser–material interaction, very little knowledge has been obtained in the past about the average atomic velocity distribution inside the shock wave. This is probably due to the large experimental difficulty in internal velocity probing. Figure 3 shows the average velocity distribution of the target materials and the gas for the computational case discussed above. Several interesting phenomena are noticed in the internal velocity distribution, and are discussed below.

In the figures at 0.025, 0.05, and 0.1 ns, a negative velocity wave is observed in the solid target. This velocity wave moves to the backside of the target. It is induced by the local stress wave. This negative velocity is not the local stress wave propagation velocity, but is related to the dislocation of the local atoms under the influence of the stress. When this velocity wave reaches the backside of the target, it just disappears and is not reflected back. This is because in the simulation a stress-absorbing boundary condition is applied on the left boundary. When the stress wave is absorbed by this special boundary condition, the net velocity of atoms disappears. This proves that our stress-absorbing boundary condition works well to eliminate the stress wave reflection.

The initial velocity of the plume in the surface region is positive due to ablation. If the plume is able to induce a shock wave, its velocity must be much higher than the sound speed of the background gas. Our study depicts that initially (0.025 ns) the ejected plume propagates with a supersonic front velocity slightly above 400 m/s which is about 3 times the sound speed in the ambient gas (132 m/s at 50 K). In the initial snapshots, it is clearly discernible that solid atoms fly out from the target with high speed accompanying intense phase explosion. The adjacent gas region is eminently compressed because the plume front pushes with great impact on the surroundings, resulting in the formation of the highly energetic shock wave. The shock wave front is already visible at 0.1 ns when the plume transfers a large portion of its kinetic energy to the shock wave, and both travel with an enormous velocity of around 350 m/s. It is important to notice that a velocity discontinuity exists at the plume/compressed gas interface. This is physically reasonable because momentum and energy transfer occurs from the ejected plume to the

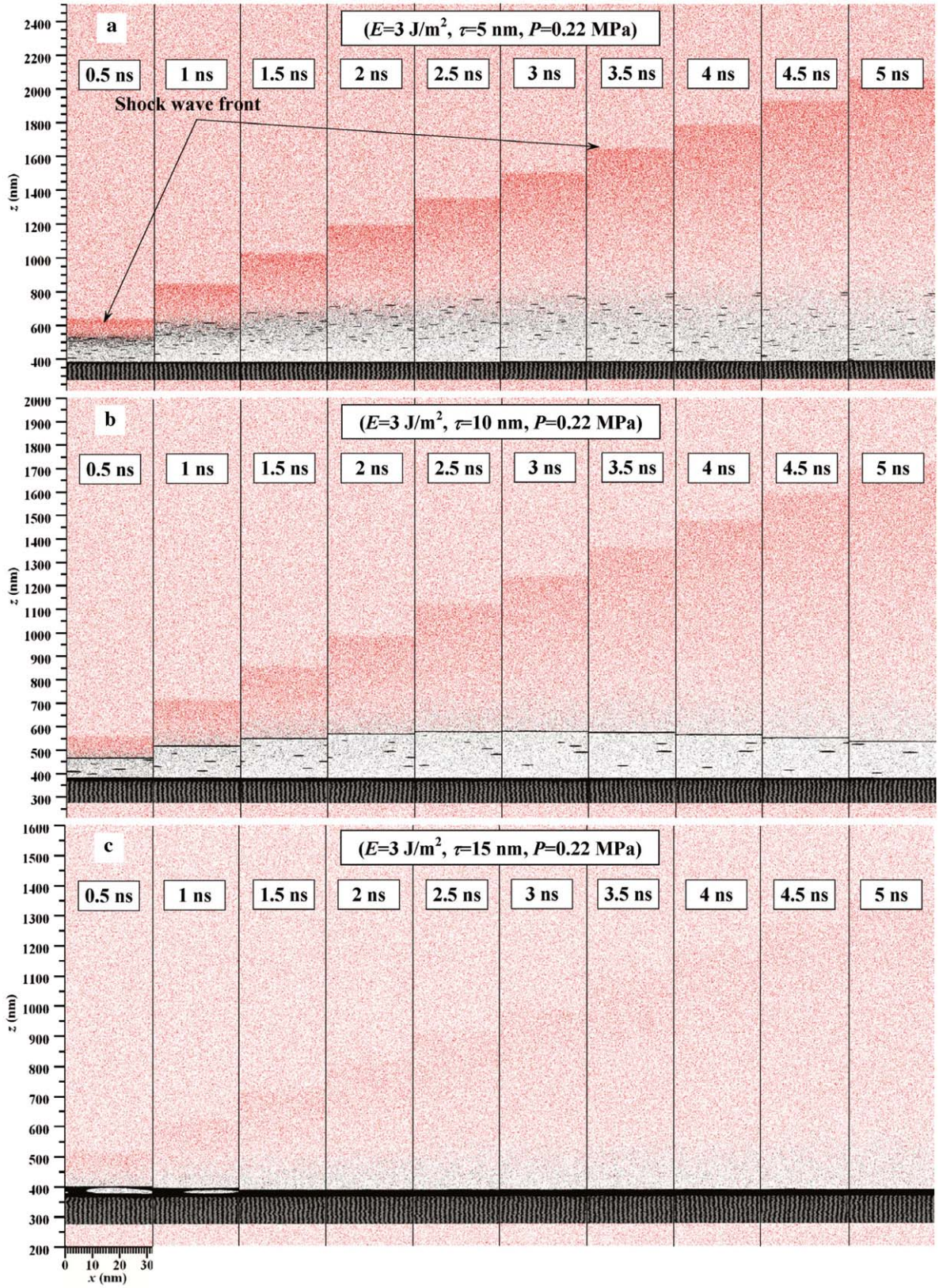

Fig. 2 A comparison of snapshots for the dynamics of shock wave formation and evolution for $E = 3$ J/m^2, at $P = 0.22$ MPa, and three different absorption depths: **a** $\tau = 5$ nm, **b** $\tau = 10$ nm, and **c** $\tau = 15$ nm. *Black*: target material; *red*: background gas

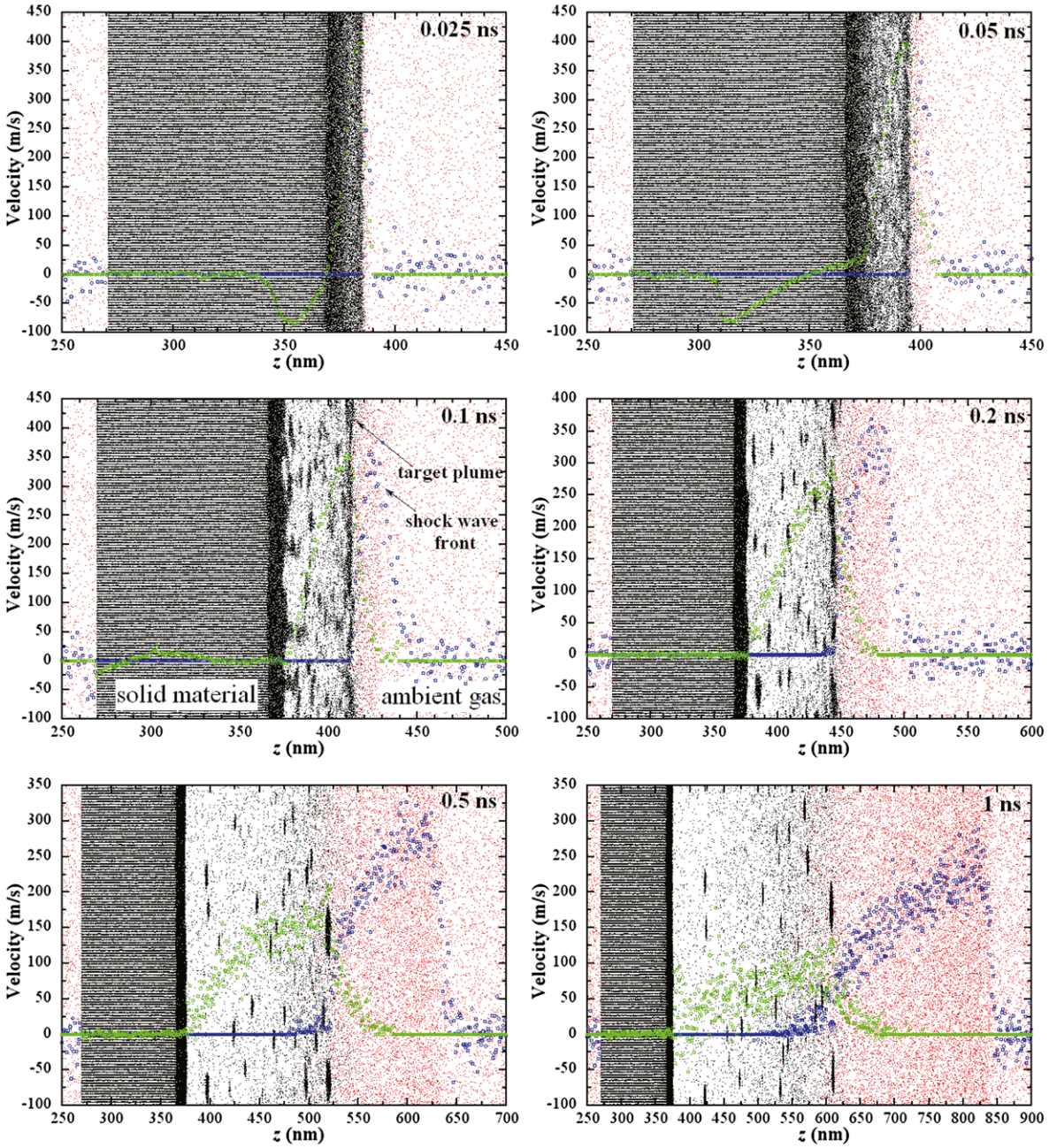

Fig. 3 Snapshots of atomic positions combined with the evolution of target and gas velocity distribution along the z-direction ($E = 3$ J/m^2, $\tau = 5$ nm, $P = 0.22$ MPa). *Green*: target material velocity; *blue*: background gas velocity; *black dots*: target atoms; *red dots*: ambient gas atoms

generated shock wave at the initial instant of time. A lot of gas atoms have been pushed out quickly with analogy to a supersonic piston. So the not-pushed or slightly-pushed gas atoms stay behind the shock wave front. This also gives rise to the non-uniform velocity distribution in the compressed ambient gas where the shock wave front features the maximum speed.

At 0.2 ns, the shock wave already gains the momentum to expand, whereas the plume begins to decelerate. At this moment, the peak velocity of atoms in the compressed ambient gas is even higher than that of the plume. Deceleration of the plume is induced by the accumulated mass of the compressed ambient gas, which becomes comparable to the plume mass. The slowdown effect by the ambient gas reduces the velocity of the expansion plume. It is interesting to notice that during the later steps it happens that the velocity of the plume becomes negative (2 to 5 ns). This means that the plume starts to move back to the target surface and could re-combine with it. The accelerated denser shock wave front propagates with a sharp velocity peak, while the

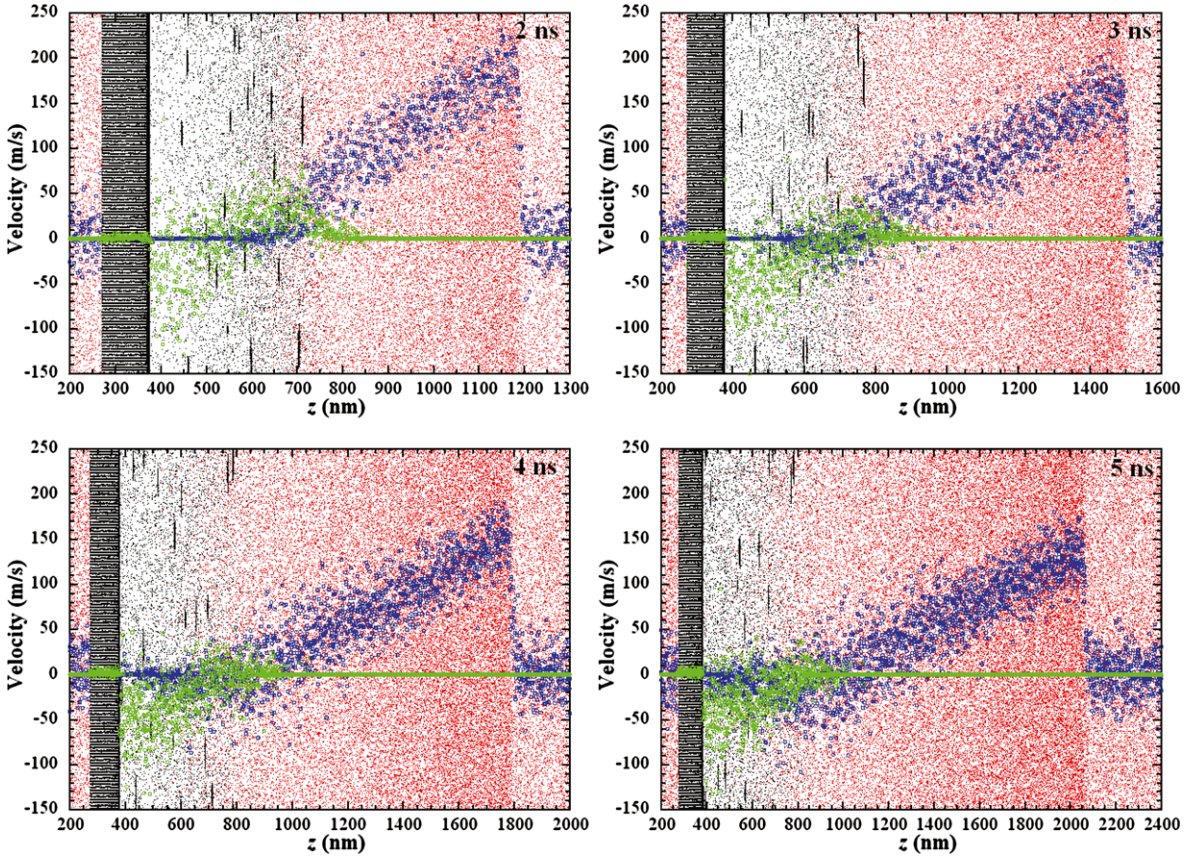

Fig. 3 (*Continued*)

rarefied 'tail' undergoes increasing scattering/diffusion with the plume constituents. It is clearly visible that deceleration and 'quenching' of the shock wave front occur due to the momentum loss to the stationary background gas. At 5 ns, the atomic velocity inside the shock wave front is very close to the sound velocity in the ambient gas (132 m/s).

3.3 The effect of laser beam absorption on shock wave

In this work, the volumetric laser energy absorption model is incorporated into the simulations. It de-emphasizes the details of laser material interaction in which quantum mechanical effects need to be taken into account. The time scale of laser energy absorption (<1 ps) is much smaller than the time scale associated with the laser pulse. Therefore, without knowing the details of laser–material interaction, the thermal and mechanical effects, as well as shock wave formation can be investigated using this absorption model [17, 19–21]. Here we present the results of simulation for optical absorption depth of 5, 10, and 15 nm which reflect the fact of different volumetric absorption of the laser beam.

Figures 2a–c show the snapshots of the dynamics and evolution of the propagating shock wave for the same laser fluence of 3 J/m^2, and the same ambient pressure of 0.22 MPa, but with different absorption depths. It is clearly visible that the absorption depth significantly affects the characteristics and generation of the shock wave. The amount of ablated material is an important parameter in laser–material interaction. The specific rate of the ablation is dependent on several factors, including laser wavelength, laser fluence, and moreover on the properties of the target material [11–13]. In the first case $\tau = 5$ nm (Fig. 2a) which has more shallow absorption depth, the shock wave forms and propagates predictably in the way as has been already described in the previous sections. Interesting and startling things occur when we increase the absorption depth. Due to the longer absorption depth, the laser beam penetrates deeper inside the sample, resulting in thicker material removal since more mass is ablated from a larger volume but with lower velocity. As it can be seen in Fig. 2b (the $\tau = 10$ nm case), a thin layer of target material is ejected out and stays mainly on the plume front. As previously stated, the background gas is extruded and pushed forward by the much higher-density plume, leading to a strong shock wave. Nanoclusters are also visible in the "tail" region of the expanding plume. Starting from 3 ns, it is very obvious that the ablated thin layer starts to move back toward the target sur-

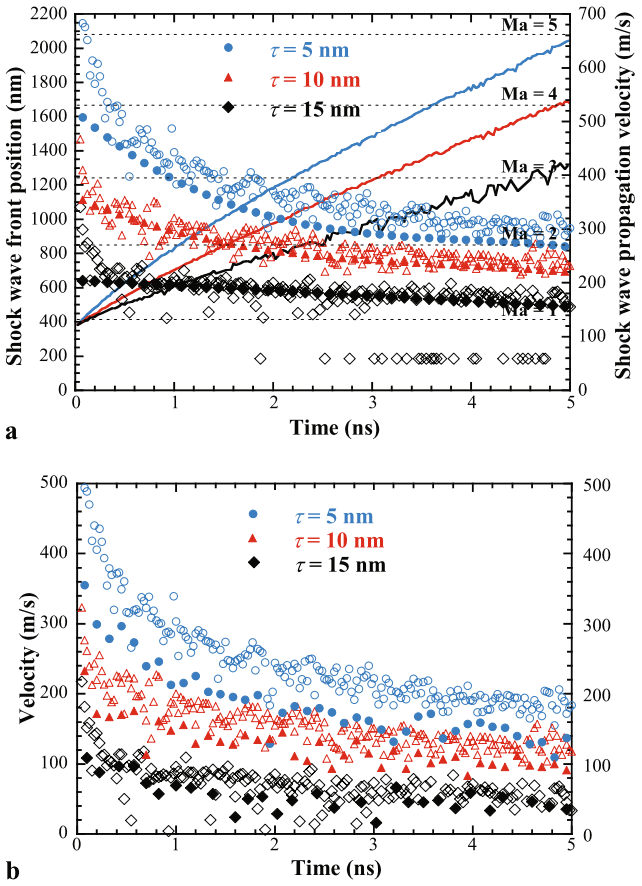

Fig. 4 A comparison of the shock wave velocities by MD vs. (8) and (9) for three absorption depths: 5 nm, 10 nm, and 15 nm, ($E = 3$ J/m^2, $P = 0.22$ MPa): **a** shock wave front position and shock wave propagation velocity; **b** mass velocity of atoms in the shock wave front. *Solid symbols*: MD velocities; *hollow symbols*: velocities from (8) and (9); *solid lines*: shock wave front position

face. This motion is caused by the high pressure in the compressed ambient gas, which prevents the nanoclusters/plume from moving out. Such phenomenon is also observed in the case of $E = 3$ J/m^2, $\tau = 5$ nm as discussed above.

Of special attention is the third case shown in Fig. 2c. When the laser absorption depth is too large (15 nm), the formation of the plume is hardly visible. At the initial stages, it is observed that a thin layer of film is ejected out a little bit (0.5 and 1 ns), and quite a large bubble forms beneath the surface. But it seems that the ejected material has not gained sufficient energy to overcome two forces: the attraction force from the molten material, and the restraint force from the ambient gas. Therefore, at 1 ns it is being pushed back, and at later steps there are only a discernible minority of particles flying out. Although a shock wave has formed, it has very low energy of propagation and it is quickly diffusing in the ambient gas, which can be noticed at 5 ns when the shock wave front becomes very difficult to distinguish.

In order to establish a further understanding of the kinetics in the nanoscale shock waves, their dynamic parameters are studied in great detail. Figure 4 is a juxtaposition of the shock wave propagation velocity, the shock wave front position (Fig. 4a), as well as mass velocity of atoms in the shock wave front (Fig. 4b), for three absorption depths. For comparison and demonstration purposes, we have marked different Mach number lines (Fig. 4a), which are multiples of the sound speed of the ambient gas (132 m/s). The shock wave thickness is the largest (1.6 μm at 5 ns) for the $\tau = 5$ nm case. The mass velocity of atoms in the shock wave front is determined by calculating the average velocity of atoms in a thin layer (about 2 nm thick) close to the shock wave front. The propagation velocity of the shock wave front is totally different from the mass velocity and is specified by using the time derivative of shock wave front position. From Fig. 4, it is seen that at 5 ns the shock wave front still propagates with a Mach number larger than 1. When the absorption depth is smaller, the shock wave front propagates faster. This is because a shorter absorption depth will result in a smaller amount of ablation, but with higher velocity, leading to a faster movement of the shock wave front. For comparison with the literature, front propagation velocity (Fig. 4a) and the mass velocity of the shock wave (Fig. 4b) are provided. The theoretical velocity distributions in that plot are based on the theoretical equations taken from [15] as

$$M = \frac{u_f}{a} = \sqrt{\frac{\gamma+1}{2\gamma}\left(\frac{p_2}{p_1}-1\right)+1} \rightarrow u_f = a\sqrt{\frac{\gamma+1}{2\gamma}\left(\frac{p_2}{p_1}-1\right)+1}, \tag{8}$$

$$u_{\mathrm{av}} = \frac{a}{\gamma}\left(\frac{p_2}{p_1}-1\right)\sqrt{\frac{\frac{2\gamma}{\gamma+1}}{\frac{p_2}{p_1}+\frac{\gamma-1}{\gamma+1}}}, \tag{9}$$

where u_f and u_{av} are shock wave propagation and mass velocity, respectively, M is the Mach number, a is the speed of sound in the ambient gas, p_1 is the ambient pressure, and $\gamma = 5/3$ is the ratio of specific heats for the ambient gas. These equations use the pressure p_2 which is the pressure of the shock wave front, and its distribution is shown in Fig. 5. This pressure is calculated based on our MD data using the following equation [17]

$$p_2 = p_{mm} = \frac{1}{\Delta V}\left(\sum_{i\neq j}^{N} r_{ij,m} F_{ij,m} + N k_{\mathrm{b}} T\right), \quad m = 1, 2, \text{ or } 3, \tag{10}$$

where ΔV is the volume of a small domain of interest, k_{b} the Boltzmann constant, and $N k_{\mathrm{b}} T$ the pressure induced by the movement of atoms. The characteristic of velocity evolution is in good agreement, despite some slight difference

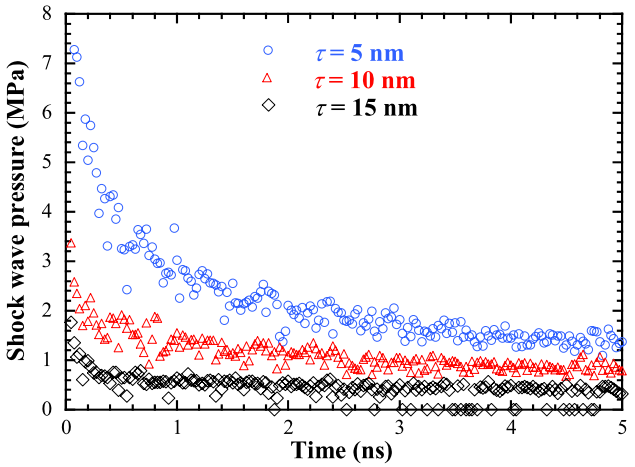

Fig. 5 Shock wave front average pressure distribution versus time for three absorption depths: 5 nm, 10 nm, and 15 nm ($E = 3$ J/m^2, $P = 0.22$ MPa)

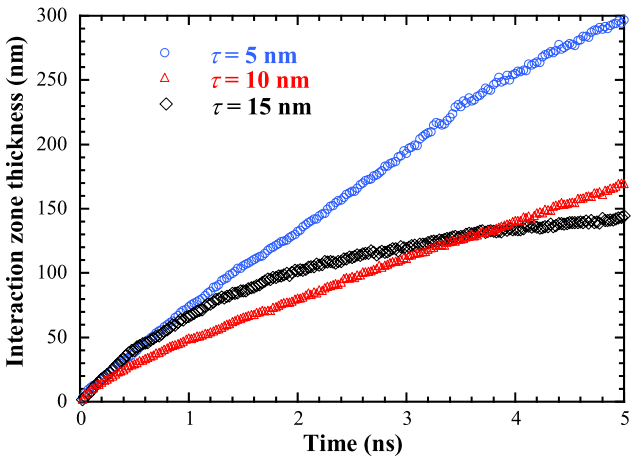

Fig. 6 Interaction zone thickness between the target and the ambient gas for three absorption depths: 5 nm, 10 nm, and 15 nm ($E = 3$ J/m^2, $P = 0.22$ MPa)

between velocity profiles obtained from cited equations and those obtained from MD simulations. These deviations are probably due to the statistical uncertainty in determining the shock wave front pressure and the position of the shock wave front. Comparing Figs. 4a and 4b, we conclude that the average mass velocity of atoms in the shock wave front is always less than the propagation speed of the shock wave front. This is because the shock wave front propagation consists of two processes: one is the movement of atoms in the shock wave front, and the other is the process to entrain the stationary adjacent ambient gas into the shock wave front to make it thicker. Therefore, the shock wave front propagation is always faster than the local mass velocity of atoms.

Another great interesting kinetic parameter which is difficult to obtain experimentally, but relatively easy to determine with MD, is the thickness of the interaction zone between the plume and background gas. The inside of the shock wave is comprised of strongly compressed background gas and fast moving plume. These two species initially will have very little mixing, and will penetrate into each other because of mass diffusion and relative movement. It is expected that strong mixing will lead to appreciable interaction between them. Figure 6 illustrates how the thickness of the interaction zone changes with time for three different absorption depths. The definition of the interaction zone thickness was detailed in Wang's previous paper [23] where it was designed in the following form

$$L_{\mathrm{mix}} = \sum \frac{n_{\mathrm{t}} \cdot n_{\mathrm{g}}}{[(n_{\mathrm{t}} + n_{\mathrm{g}})/2]^2} \cdot \delta z, \tag{11}$$

where $n_{\mathrm{t}} = N_{\mathrm{target}}/(N_{\mathrm{target}} + N_{\mathrm{gas}})$ and $n_{\mathrm{g}} = N_{\mathrm{gas}}/(N_{\mathrm{target}} + N_{\mathrm{gas}})$. Symbols n_{t} and n_{g} denote the fractions of the target and gas atoms in a small layer δz. N_{target} and N_{gas} are the numbers of target and gas atoms in a thin layer, respectively. Generally speaking, when the optical absorption depth is smaller, the shock wave features a much larger interaction zone between the plume and the ambient gas. This is due to the faster movement of the plume, which makes it possible for the plume atoms to penetrate more into the ambient gas. In our past work, it has been proven that the increase of the interaction zone thickness is largely due to the relative movement between the plume and gas atoms [23]. For $\tau = 5$ nm and $\tau = 10$ nm, the thickness changes almost linearly with time. In the situation when a thin layer film is ejected, the density of the plume front is large, but it does not allow penetration by scattered background gas constituents (the $\tau = 10$ nm case). Therefore, only the small clusters/particles in front of this layer mix with the ambient gas molecules. This results in a relative small interaction zone between the plume and background gas. For the case $\tau = 15$ nm, it is predictable that the interaction zone is close to saturation at very early stages owing to the weakness of the plume and the shock wave.

3.4 The effect of ambient pressure on shock wave

Changing of the ambient pressure distinctly affects the controlling parameters of the plume characteristics, such as spatial distribution, deposition rate, and kinetic energy distribution of the depositing species, which greatly vary due to plume scattering, attenuation, and thermalization [3]. Figure 7 displays snapshots of the spatial plume and shock wave evolution under three different ambient pressures and $E = 5$ J/m^2, $\tau = 5$ nm. It is evident that raising the background gas pressure results in denser shock wave formation, greater strength, and considerable sharpening of its front. In fact, an increase in the ambient pressure strengthens interpenetration collisions on the plume expansion front with the

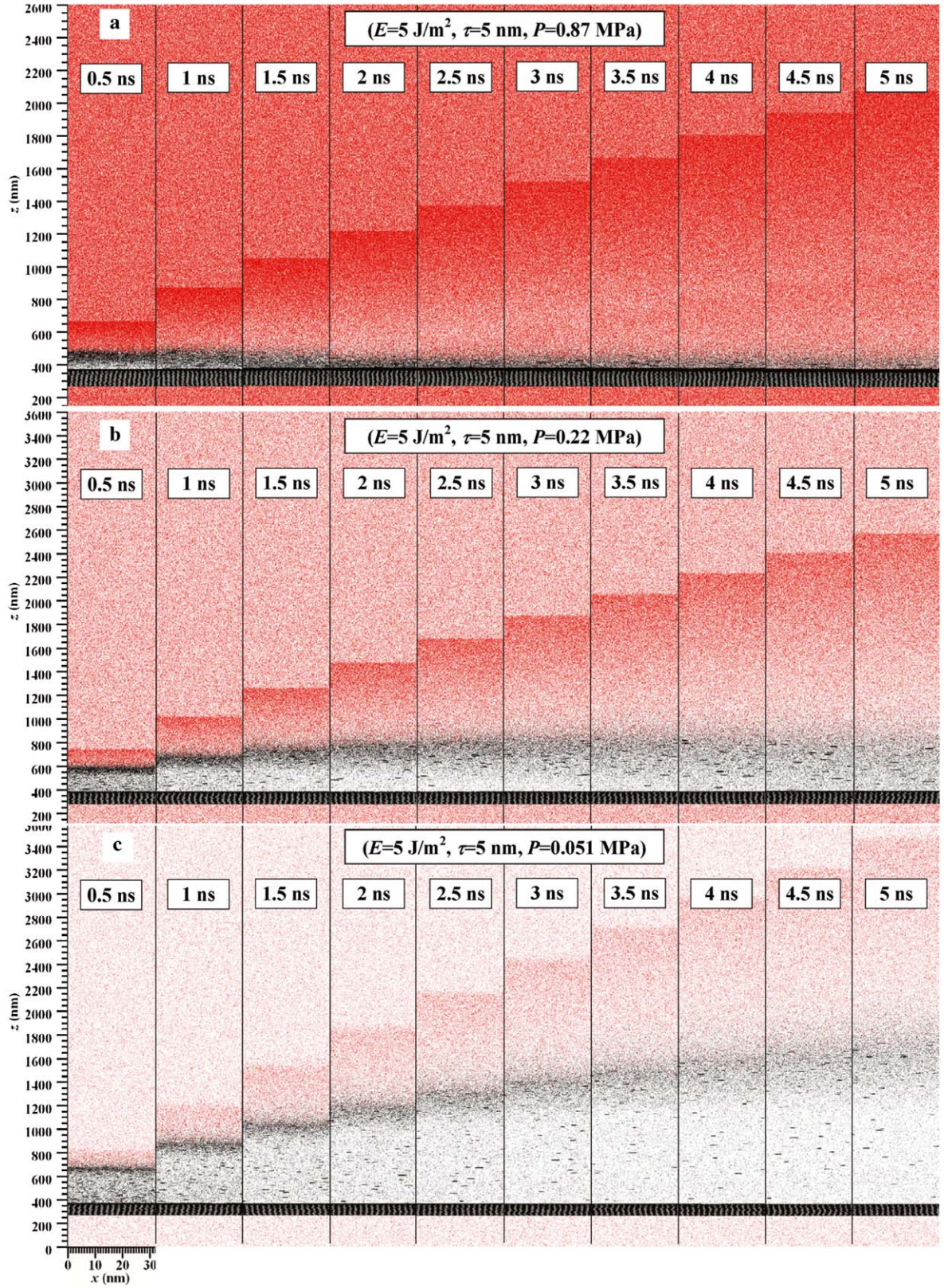

Fig. 7 A comparison of snapshots for the dynamics of shock wave formation and evolution for $E = 5\ \mathrm{J/m^2}$, $\tau = 5$ nm, and three different ambient pressures: **a** $P = 0.87$ MPa, **b** $P = 0.22$ MPa, and **c** $P = 0.051$ MPa

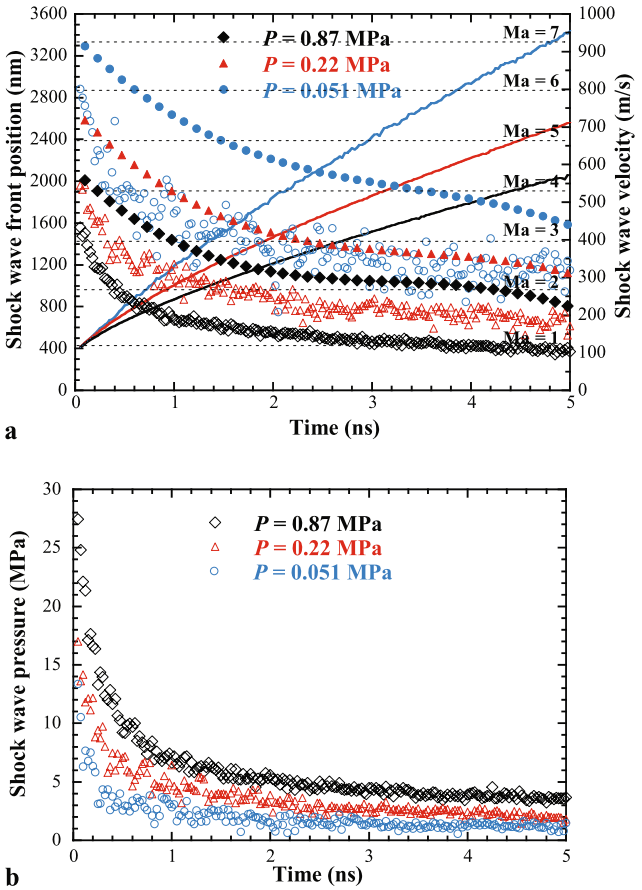

Fig. 8 **a** Position, shock wave propagation velocity, and the mass velocity of atoms in the shock wave front for three ambient pressures: 0.87 MPa, 0.22 MPa, 0.051 MPa ($E = 5$ J/m^2, $\tau = 5$ nm). (*Solid symbols*: shock wave front propagation velocity; *hollow symbols*: mass velocity in the shock wave front; *solid lines*: shock wave front position); **b** Shock wave front average pressure distribution in time for three ambient pressures: 0.87 MPa, 0.22 MPa, 0.051 MPa ($E = 5$ J/m^2, $\tau = 5$ nm)

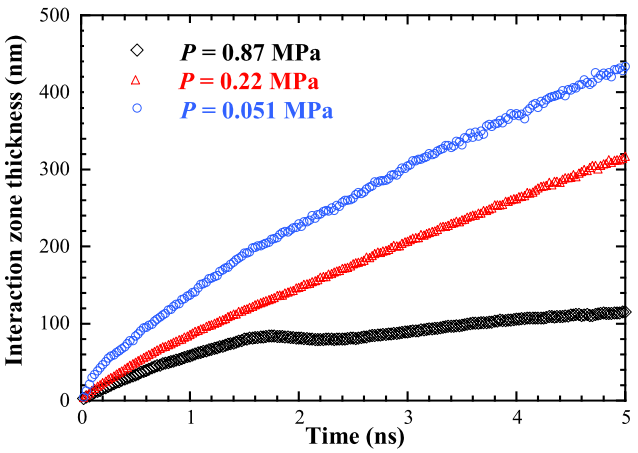

Fig. 9 Interaction zone thickness between the target and the ambient gas for three ambient pressures: 0.87 MPa, 0.22 MPa, 0.051 MPa ($E = 5$ J/m^2, $\tau = 5$ nm)

background gas. When the pressure is 0.87 MPa, it is obvious that the plume does not expand much to the space. Starting from 1 ns, the plume moves back to the liquid surface. At 5 ns, only very little plume is observed in space. Such back movement of the plume is also observed for 0.22 MPa, but happens much later (starting from 3.5 ns). Much more plume is ejected when the ambient pressure is 0.22 MPa. Stronger forward movement of the plume in lower pressure is more obvious when it is reduced to 0.051 MPa, when the plume flies into the space as much as 1.6 μm at 5 ns.

In order to extract more valuable information about the ambient pressure effect on the shock wave dynamics, Fig. 8 is provided to illustrate the shock wave propagation velocity, the mass velocity of atoms in the shock wave front, the shock wave front position for three background gas pressures (Fig. 8a), and shock wave front average pressure distribution in time (Fig. 8b). It can be inferred that the shock wave forward-directed length is much larger (around 3 μm at 5 ns) when the ambient pressure is lower (0.051 MPa), which is visible both in Fig. 8a and in Fig. 7c. It is justifiable that the shock wave expands further when the pressure drops because the ambient gas constrains its expansion less. Furthermore, the shock wave propagation velocity becomes higher when the ambient pressure declines and it can reach an immense initial Mach number of 7 for 0.051 MPa pressure (Fig. 8b). The reason is that the shock wave expands more freely under low ambient pressure, and gains higher velocity in lower background pressure due to the less collisional interaction between the gas atoms trapped in the shock front and the ambient gas.

It can also be observed that the shock wave slowing down effect is stronger when raising the ambient pressure. As the background pressure increases, the shock wave front undergoes larger scattering and is more attenuated by background gas collisions. When the ambient pressure is higher, the formed shock wave front features a much higher pressure, initially close to 30 MPa under the ambient pressure of 0.87 MPa. As the expansion progresses, the velocity in the shock wave front continues to decrease, the shock pressure is reduced noticeably, and the shielded slower components propagate to coalesce with the slowed material on the contact plume front [3]. This results in an increase of the interaction zone thickness which is presented in Fig. 9. In general, the mixing length (interaction zone thickness) is larger when the ambient pressure declines. This is because of the higher plume propagation velocity and consequently higher recombination process of the plume constituents with shielded slower components of the shock wave. Despite almost linear increasing character of the mixing length at lower pressures (0.051 MPa and 0.22 MPa), very surprising things occur for the higher pressure 0.87 MPa. It looks like the process of mixing is somehow interrupted at 1.5 ns. A close look at Fig. 7a reveals that at 1.5 ns a large amount of plume is

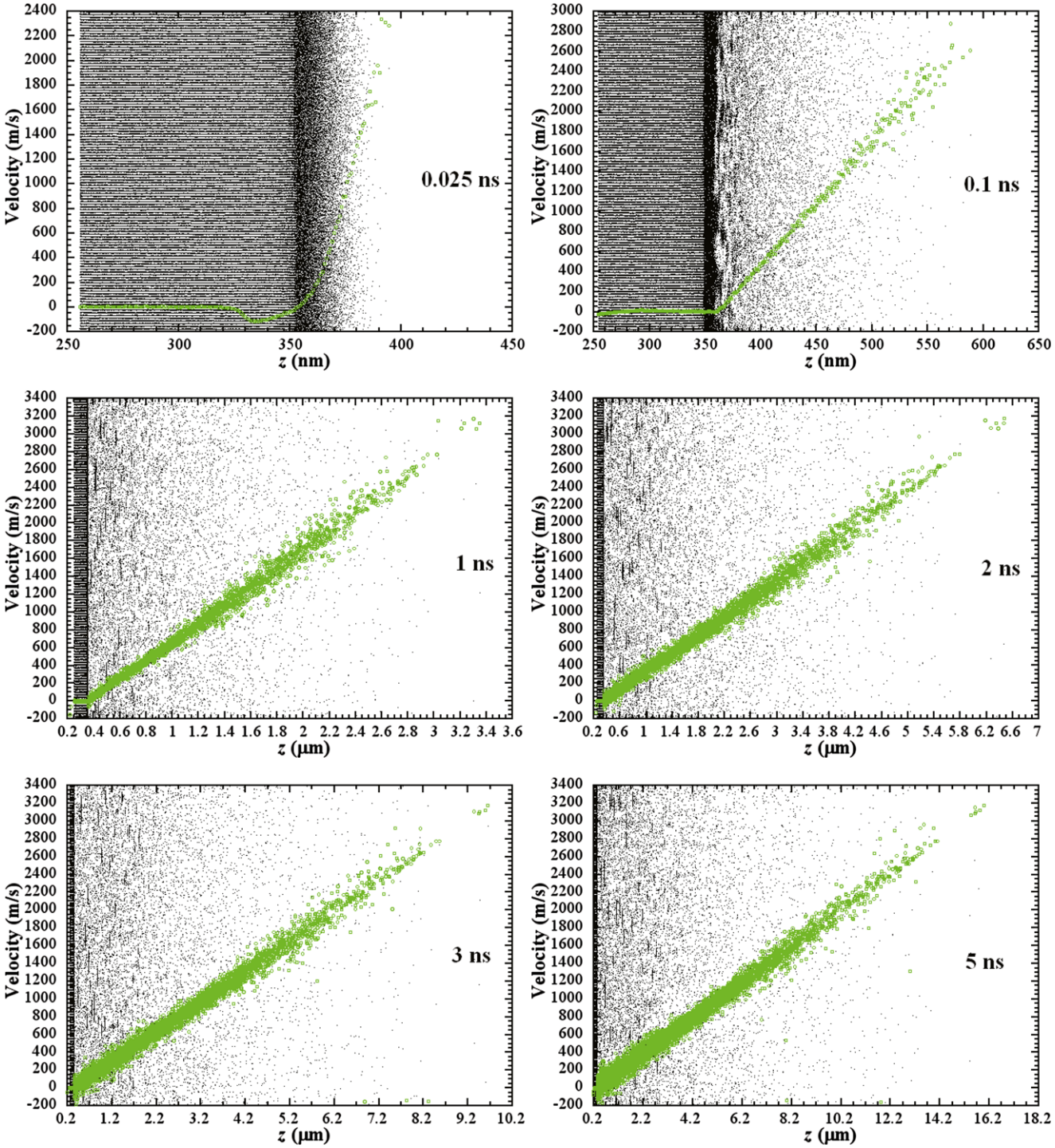

Fig. 10 Snapshots of atomic positions combined with the evolution of target velocity distribution along the z-direction in vacuum ($E = 5$ J/m^2, $\tau = 5$ nm). *Green*: target material velocity; *black dots*: target atoms

pushed back to recombine with the liquid surface. Therefore, this reduces the interaction zone thickness between the plume and the ambient gas. The increase of the interaction zone thickness after 1.5 ns is mainly attributed to the slow diffusion of the plume species into the ambient gas. The experimental work of the pressure influence on the laser ablation process has been widely covered in the literature [3, 10]. Our work shows sound agreement with the experiments in terms of the shock wave and plume characteristics and behavior.

3.5 A comparison with laser–material interaction in vacuum

For the purpose of comparison, the situation resembling the plume expansion in a vacuum is presented. This represents the extreme situation of the pressure effect (zero ambient pressure). The material plume expands freely in the vacuum since there is no medium to constrain its propagation. Figure 10 illustrates the spatial plume development in vacuum combined with the evolution of the target velocity along the z-direction for similar laser ablation process parameters as previously applied: laser fluence of 5 J/m^2 and optical absorption depth of 5 nm. It can be noticed that the furthest flying out material particles can reach a length range of 16 μm at 5 ns from the target surface. To be able to attain such a far distance within an ultrashort period of time, they must have very high velocity. As it can be seen in Fig. 10, the fastest traveling plume components can achieve extremely high expansion velocities near 3200 m/s, which approach closely the experimental velocity range, see, for instance, in [9].

Having shown knowledge of shock wave expansion and evolution, it would be of considerable significance to also gain an insight into plume dynamics. Figure 11 displays the position of the plume front at three background pressures and under vacuum conditions. In our work, the plume front has been determined on the basis of plume density. When scanning layer by layer from the top of the whole domain, it will encounter an increasing number of ejectants from the target material. By selecting the criterion (dependent on the specific case since the number of atoms in the plume front will vary when the ambient condition changes) the position of the plume front can be determined. It is clear that apparent difference arises between the plume expansion in vacuum and in the presence of ambient gas. The plume front in vacuum rises very fast in comparison to the cases of ambient pressure, indicating linear free expansion in vacuum. On the other hand, as the pressure of the ambient gas increases, the plume becomes more constrained, which results in the reduction of the effective length of the plume. Our results show a perceivable analogy to the experimental outcomes described by Harilal et al. [10] for nanosecond laser–material interaction (Nd:YAG laser, 8 ns pulse width). The inset of Fig. 11 may serve comparison purpose. Although this work's simulation conditions differ from those of [10] in time scale and material, close agreement is observed between them in plume's propagation trend considering the effect of ambient pressure. Evidently, the plume development using MD simulations is not complete due to the high computational cost and can be tracked only up to a few nanoseconds. However, similarity at the early stage of evolution can be attributed, when comparing the $p = 0.051$ MPa curve with the experimental curve at 100 Torr (0.015 MPa), the closest pressure condition, where one can quickly notice the apparent, and expected for later times, analogous behavior. Moreover, even though the timescale in MD simulation is three-orders smaller than that in the experiment using nanosecond laser, the reported dynamic evolution of shock waves reveals the early stage physics for shock wave formation and evolution in picosecond laser–material interaction.

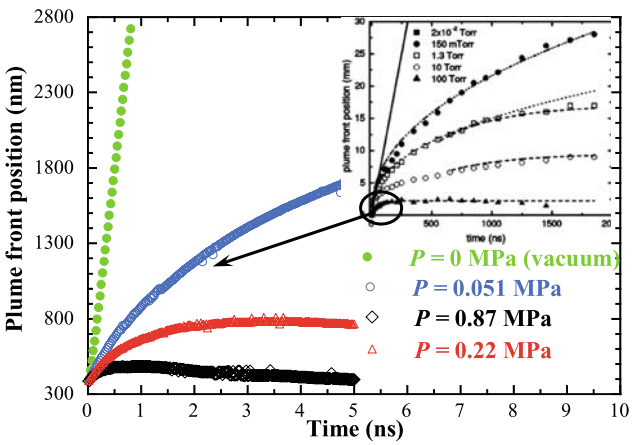

Fig. 11 Position of the plume front ($E = 5$ J/m^2, $\tau = 5$ nm) for three ambient pressures: 0.87 MPa, 0.22 MPa, 0.051 MPa and comparison with vacuum conditions. The *inset* in the figure shows position–time plots of the luminous front of the aluminum plume produced at different background air pressures taken from [10]

For the pressure of 0.051 MPa, the plume expands invariably forward from the surface within the computational time, which can be observed in Fig. 11 or in Fig. 7c. When the background gas pressure increases, the strong shock wave stops the movement of plume and makes it move toward the target surface. As the plume expands, the counteraction of the higher pressure ambient gas increases and the contact surface slows down, resulting in backward motion. This is observed for the background gas pressure of 0.87 MPa and 0.22 MPa in Fig. 11. For the ambient gas pressure of 0.22 MPa, the plume starts being pushed to the surface at 3.5 ns. Very perceivable backward movement is observed for the case with the highest ambient pressure (0.87 MPa). Just after 1.5 ns, the plume is mercilessly knocked back and recombines with the target surface. The plume backward motion can lead to intensification of the surface redeposition process. As observed in experiments [26], the mass of the redeposited debris goes up with an increase in the background pressure. This is because for a higher pressure the entrapment of the particles is stronger due to the higher gas density, consequently dragging more ablated mass back to the target surface. As long as the backward movement of the plume makes it redeposit on the target surface, a series of thermodynamic processes will occur (e.g., condensation and solidification). The local temperature and pressure play important roles in these processes. Further study is underway to investigate the phase change after plume redeposition.

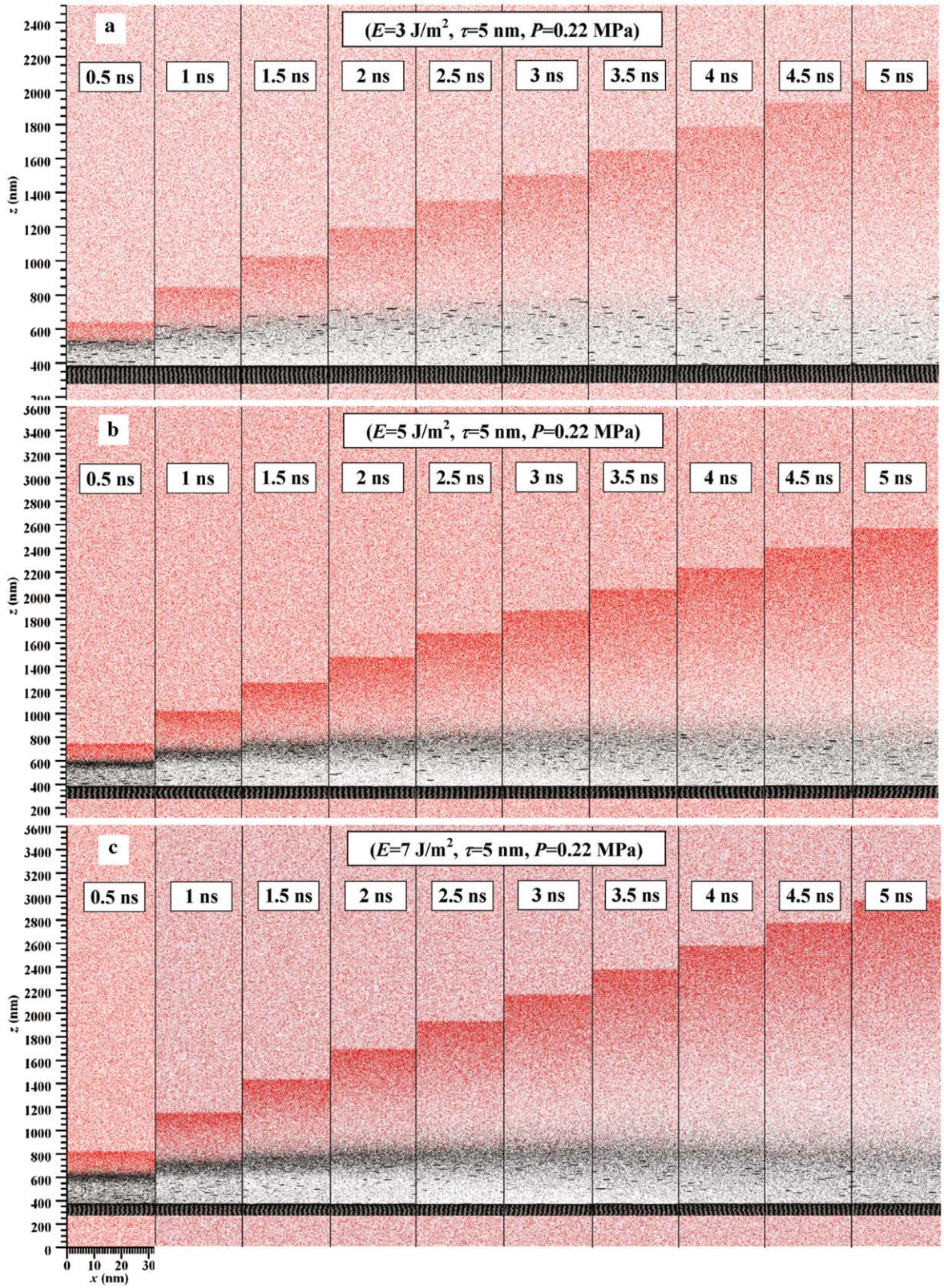

Fig. 12 A comparison of snapshots for the dynamics of shock wave formation and evolution for $P = 0.22$ MPa, $\tau = 5$ nm, and three different laser fluences: **a** $E = 3$ J/m^2, **b** $E = 5$ J/m^2, and **c** $E = 7$ J/m^2

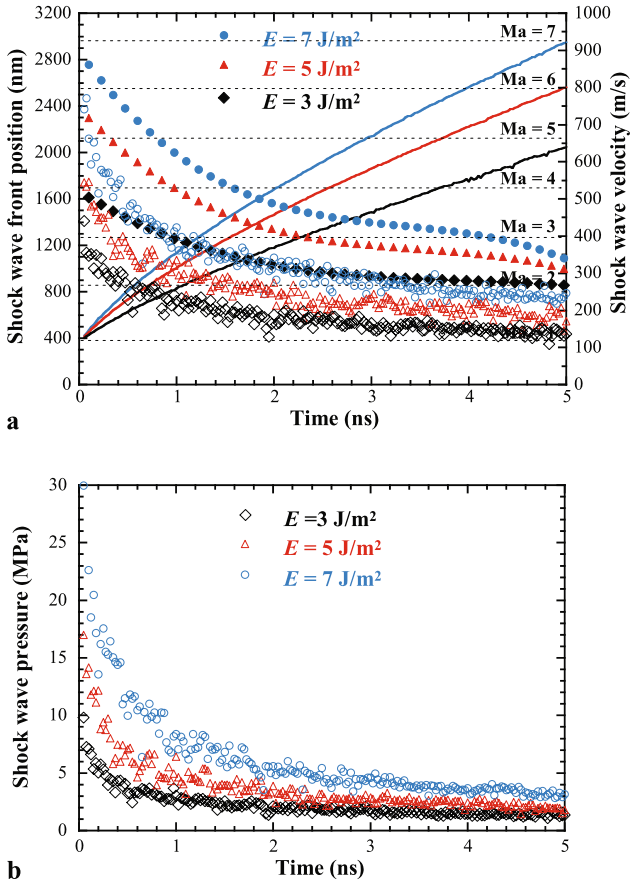

Fig. 13 **a** Position, shock wave propagation velocity, and the mass velocity of atoms in the shock wave front for three laser fluences: 3 J/m^2, 5 J/m^2, 7 J/m^2 ($P = 0.22$ MPa, $\tau = 5$ nm). (*Solid symbols*: shock wave front propagation velocity; *hollow symbols*: mass velocity in the shock wave front; *solid lines*: shock wave front position); **b** Shock wave front average pressure distribution in time for three laser fluences: 3 J/m^2, 5 J/m^2, 7 J/m^2 ($P = 0.22$ MPa, $\tau = 5$ nm)

3.6 The effect of laser fluence on shock wave

In laser ablation process, it is important to efficiently ablate material without excessive overheating and melting of the sample. The fact is that for different materials there exists a certain level of laser energy, often called a threshold fluence of ablation, above which the material is expelled from the target surface. With increased irradiance above the ablation threshold, the ejected plume becomes more intense and the generated shock wave becomes stronger. In this work, the dependence of the ablation process on the laser fluence is shown on the basis of three laser energy levels: 3, 5, and 7 J/m^2 when $\tau = 5$ nm, and $P = 0.22$ MPa. The atomic positions and dynamics of the plume and shock wave evolution are presented in Fig. 12. Figure 13 shows the velocity (Fig. 13a) and pressure evolution (Fig. 13b) at the shock wave front for the scenarios shown in Fig. 12. From Fig. 12, it is observed that with increasing laser energy input the plume becomes more uniform with fewer large particles ablated out. When the laser fluence is higher, the material is ablated out suddenly in a more concentrated time, leading to a more concentrated plume front.

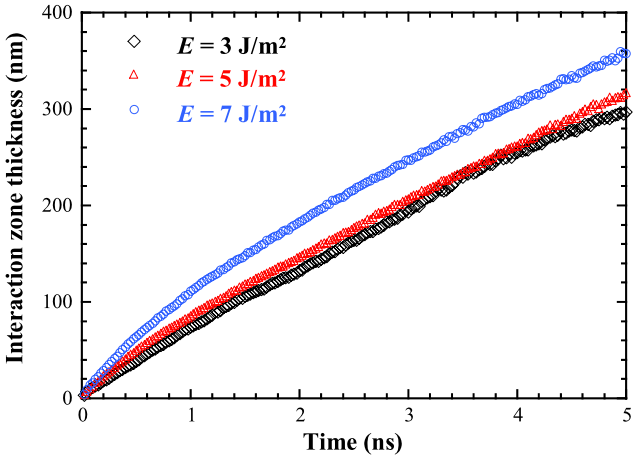

Fig. 14 Interaction zone thickness between the target and the ambient gas for three laser fluences: 3 J/m^2, 5 J/m^2, 7 J/m^2 ($P = 0.22$ MPa, $\tau = 5$ nm)

More distant shock wave propagation is visible when the laser fluence is higher (Figs. 12 and 13a). Furthermore, a higher shock wave propagation velocity and pressure for 7 J/m^2 case indicates that the larger amount of laser energy generates a much stronger shock wave (Figs. 12 and 13). The interaction zone thickness also increases when the laser fluence is increased. This is due to greater relative movement of the plume and gas particles (Fig. 14). It can also be inferred that, the higher laser pulse energies cause an increase in the ablated mass, additionally resulting in a larger material depth removed. That occurrence is presented experimentally [11, 26] and is in close agreement with our results. Related analysis of the composition and density of the ejected plume on the laser fluence dependence has been also recently performed using MD simulations [18]. For applied fluence ranges, the results obtained here and observations are correspondingly reasonable.

4 Conclusions

In this work, MD simulations were carried out to study the dynamics, internal structure, and the evolution of shock waves in picosecond laser–material interaction, while emphasis was placed on the effect of the laser absorption depth, ambient pressure, and laser fluence. Our study showed that the initial shock wave propagation velocity can reach an enormous value close to 7 Mach, and the initial pressure can go even over 25 MPa. The MD results on shock wave propagation and mass velocity were in sound agreement with the theoretical prediction, demonstrating the validity of the

MD approach for studying shock waves in laser–material interaction. At the interface between the plume and the compressed ambient gas, a velocity discontinuity was observed. Owing to the strong constraint from the compressed ambient gas, during the late stage the ablated plume either stopped moving forward and mixed with the ambient gas, or moved backward to the target surface, leading to surface debris redeposition. It was found that smaller laser absorption depth, lower ambient pressure, or higher laser fluence would lead to stronger shock waves which were featured with faster propagation in space and thicker interaction zone between the target and ambient gas.

Acknowledgements Support for this work from the start-up fund of Iowa State University is gratefully acknowledged. Partial support for this work from NSF (CMS: 0457471), Air Force Office for Scientific Research and MURI from ONR is gratefully acknowledged.

References

1. E. Fogarassy, S. Lazare (eds.), *Laser Ablation of Electronic Materials* (North-Holland, Amsterdam, 1992)
2. S.A. Darke, J.F. Tyson, J. Anal. At. Spectrom. **8**, 145–209 (1993)
3. D.B. Chrisey, G.K. Hubler (eds.), *Pulsed Laser Deposition of Thin Films* (Wiley, New York, 1994)
4. H.C. Le, D.E. Zeitun, J.D. Parisse, M. Sentis, W. Marine, Phys. Rev. E **62**, 4152–4161 (2000)
5. D.B. Geohegan, A.A. Puretzky, Appl. Phys. Lett. **67**, 197–199 (1995)
6. D.B. Geohegan, A.A. Puretzky, Appl. Surf. Sci. **96–98**, 131–138 (1996)
7. J.N. Leboeuf, K.R. Chen, J.M. Donato, D.B. Geohegan, C.L. Liu, A.A. Puretzky, R.F. Wood, Phys. Plasmas **3**, 2203–2206 (1996)
8. R.F. Wood, K.R. Chen, J.N. Leboeuf, A.A. Puretzky, D.B. Geohegan, Phys. Rev. Lett. **79**, 1571–1574 (1997)
9. A.A. Voevodin, J.G. Jones, J.S. Zabinski, J. Appl. Phys. **88**, 1088–1096 (2000)
10. S.S. Harilal, C.V. Bindhu, M.S. Tillack, F. Najmabadi, A.C. Gaeris, J. Appl. Phys. **93**, 2380–2388 (2003)
11. P.R.D. Mason, A.J.G. Mank, J. Anal. At. Spectrom. **16**, 1381–1388 (2001)
12. R.E. Russo, X.L. Mao, O.V. Borisov, H. Liu, J. Anal. At. Spectrom. **15**, 1115–1120 (2000)
13. R.E. Russo, X. Mao, J.J. Gonzales, S.S. Mao, J. Anal. At. Spectrom. **17**, 1072–1075 (2002)
14. A.V. Bulgakov, N.M. Bulgakova, J. Phys. D: Appl. Phys. **28**, 1710–1718 (1995)
15. Z. Zhang, G. Gogos, Phys. Rev. B **69**, 235403 (2004)
16. A.V. Bulgakov, N.M. Bulgakova, J. Phys. D: Appl. Phys. **31**, 693–703 (1998)
17. X. Wang, J. Phys. D: Appl. Phys. **38**, 1805–1823 (2005)
18. L.V. Zhigilei, E. Leveugle, B.J. Garrison, Y.G. Yingling, M.I. Zeifman, Chem. Rev. **103**, 321–347 (2003)
19. X. Wang, X. Xu, J. Heat Transf. ASME **124**, 265–274 (2002)
20. X. Wang, X. Xu, Int. J. Heat Transf. **46**, 45–53 (2003)
21. X. Wang, X. Xu, J. Heat Transf. ASME **125**, 1147–1155 (2003)
22. X. Feng, X. Wang, Phys. Lett. A **369**, 323–327 (2007)
23. L. Zhang, X. Wang, Jpn. J. Appl. Phys. **47**, 964–968 (2008)
24. L.V. Zhigilei, B.J. Garrison, Mater. Res. Soc. Symp. Proc. **538**, 491–496 (1999)
25. M.P. Allen, D.J. Tildesley, *Computer Simulation of Liquids* (Clarendon Press, Oxford, 1987)
26. S. Singh, M. Argument, Y.Y. Tsui, R. Fedosejevs, J. Appl. Phys. **98**, 113520 (2005)